Hindawi
Journal of Nanomaterials
Volume 2019, Article ID 9807605, 12 pages
https://doi.org/10.1155/2019/9807605

Research Article

Removal of Synthetic Azo Dye Using Bimetallic Nickel-Iron Nanoparticles

Shelby L. Foster,[1] Katie Estoque,[2] Michael Voecks,[3] Nikki Rentz,[4] and Lauren F. Greenlee[1]

[1]*Ralph E. Martin Department of Chemical Engineering, University of Arkansas, Fayetteville AR, USA*
[2]*Department of Chemistry and Chemical Biology, Cornell University, Ithaca NY, USA*
[3]*Department of Computer Science, University of Colorado Boulder, Boulder CO, USA*
[4]*National Institute of Standards and Technology, Boulder CO, USA*

Correspondence should be addressed to Lauren F. Greenlee; greenlee@uark.edu

Received 22 September 2018; Accepted 12 February 2019; Published 19 March 2019

Academic Editor: Victor M. Castaño

Bimetallic nanoparticles comprised of iron (Fe) and nickel (Ni) were investigated for the removal of an azo dye contaminant in water. Morphology (core shell and alloy) and metal molar ratio (Ni_2Fe_{10}, Ni_5Fe_{10}, and $Ni_{10}Fe_{10}$) were tested as key nanoparticle properties. The shelf life of the nanoparticles was tested over a 3-week period, and the effect of initial nanoparticle concentration on dye removal was evaluated. The highest initial nanoparticle concentration (1000 mg/L) showed consistent Orange G removal and the greatest extent of dye removal, as compared to the other tested concentrations (i.e., 750 mg/L, 500 mg/L, and 250 mg/L) for the same nanoparticle morphology and metal molar ratio. The metal molar ratio significantly affected the performance of the core shell morphology, where overall dye removal was found to be 66%, 89%, and 98% with an increasing molar ratio ($Ni_2Fe_{10} \rightarrow Ni_5Fe_{10} \rightarrow Ni_{10}Fe_{10}$). In contrast, the overall removal of the dye for all molar ratios of the alloy nanoparticles only resulted in a variability of ±0.005%. When stored in water for 3 weeks, core shell nanoparticles lost reactivity with an average > 17% loss in removal with each passing week. However, the alloy nanoparticles were able to continually remove Orange G from solution after 3 weeks of storage to ~97% when used at a starting nanoparticle concentration of 1000 mg/L. Overall, the Ni_2Fe_{10}, Ni_5Fe_{10}, and $Ni_{10}Fe_{10}$ alloy nanoparticles with a starting nanoparticle concentration of 1000 mg/L resulted in the greatest dye removal of 97%, 99%, and 98%, respectively. Kinetic rate models were used to analyze dye removal rate constants as a function of nanoparticle properties. Kinetic rate models were seen to differ from core shell (first-order kinetics) to alloy morphology (second-order kinetics). Alloy nanoparticles resulted in as high as *X* kinetic rate constant, and core shell nanoparticles resulted in as high as XX kinetic rate constant. Metal leaching from the nanoparticles was investigated; alloy nanoparticles resulted in leaching of 3% Fe and 5% Ni which is similar to core shell leaching of 3.2% Fe and 4.3% Ni from the $Fe_{10}Ni_{10}$ nanoparticles.

1. Introduction

The growth of the world population over the last decade is a result of increasing technological, economical, and industrial success. As large, established countries, like the United States, China, and others, have optimized mass production of living necessities, populations have been able to grow with affordable access to commodities. However, the rise of commodity mass production also produces waste products that harm ecosystems and natural environments. One such offender to local water environments is the textile industry. A textile plant manufacturing of 20,000 lb/day of fabric consumes 36,000 lb/day of water on average [1]. The required use of water as a solvent for processing chemicals, washing and rinsing fabrics, and the cooling of mechanical equipment amounts for 5% of the textile industry's production cost [1]. The inefficiency of the dying process requires an excess of 10 lb of water to every 1 lb of fabric, leading upwards to 200,000 tons of dye lost to effluent each year [2, 3].

One of the most common classes of dyes used in the textile industry is azo dyes. Azo dyes comprise 60-70% of all of the inorganic dyes manufactured in the world, making

them the largest group of colorants in textile effluents. Azo dyes have been shown to be toxic [4], mutagenic [5], and potential carcinogens [6]. The degradation of azo dyes is commonly done through concerted oxidation and reduction reactions [7, 8] to release an aromatic amine group; however, aromatic amines have been tied to cancer [6, 9]. These dyes are comprised of a double nitrogen bond with aryl functional groups attached on both sides of the nitrogen bond. Orange G is a nontoxic synthetic azo dye bearing a similar chemical structure, thus making the dye an ideal model contaminant molecule to study and understand the potential success of experimental dye contaminant removal approaches. Further, dye molecules such as Orange G have similar molecular structural components (e.g., benzene rings) as other water contaminants and are useful to study as a spectroscopically measurable contaminant model in synthetic wastewater studies.

Physical, chemical, and biological processes, including microbial degradation, filtration, and membrane separation, have been utilized to treat contaminated water [10, 11]. Unfortunately, most of these methods involve high cost and poor removal efficiency. Specifically, for industrial dye removal, physical and chemical methods such as Fenton's reagent, electrochemical destruction, adsorbent materials, and catalytic reductive processes have been investigated [12–17]. Fenton's reagent is an effective decolorization method for both soluble and insoluble dyes but generates sludge as a side product [18]. Electrochemical destruction adequately breaks down the dye compound into nonhazardous products but is limited by the high cost of electricity [18]. Activated carbon removes a wide variety of dyes through adsorption. While activated carbon can be regenerated for further use, the process results in a loss of carbon and an increase in overall cost [19]. Zero-valent iron (ZVI) has become prevalent in water treatment processes as a nontoxic, inexpensive, and environmentally compatible material [20, 21]. ZVI combines adsorption, reduction, and oxidation methods to effectively breakdown and remove contaminants. ZVI has been a focus of investigation for a few decades and has been found as an effective reducing agent for azo dyes when in aqueous solution [22]. Recently, nanoscale zero-valent iron (nZVI) has received attention in water treatment due to the high specific surface area, small particle size, and reactivity [23]. nZVI was shown to decolor dye effectively over a range of pH through a rapid first-order kinetic process [24]. However, the reactivity of nZVI leads to a decreased lifetime. Therefore, incorporation of second metal, such as nickel, has been used as a successful approach to aid in stability while maintaining effective dye removal [8, 25].

Specifically for azo dye removal and degradation, the addition of Ni has been shown to result in an increase in catalytic lifetime of up to 10 days [8] and utilization of the corrosion of Fe to enhance reduction with the formation of nickel hydride [26]. Through investigations, it has been shown that as the initial concentration of azo dye is increased, degradation becomes slower, and as the initial concentration of nanoparticles increases, azo dye degradation increases [8, 26–30]. Azo dye degradation with bimetallic NiFe nanoparticles has been shown to work more effectively at lower pH values [8, 26–28] and has shown quicker initial degradation at increased temperatures as high as 40°C [26, 27]. The current literature focuses on bimetallic alloy morphology and lacks an understanding of how a core shell morphology can affect azo dye degradation and nanoparticle lifetime. There is also a lack of investigation of how NiFe molar ratio affects azo dye degradation, leading to investigation across papers where characteristics other than molar ratio are also changing. This variation of multiple nanoparticle properties makes comparison across studies, or understanding how metal molar ratio impacts removal, difficult.

In this work, novel nanoparticle bimetallic composition and nanoparticle morphology of aqueous batch synthesized NiFe nanoparticles are explored to determine the effect of these nanoparticle properties on the removal of the model azo dye, Orange G, from aqueous dye solutions. The storage shelf life of these bimetallic nanoparticles is also investigated. The effects of these properties are analyzed as a function of nanoparticle concentration and over time, and the results from dye removal studies are modeled to understand how the kinetics of dye removal is impacted by each property.

2. Materials and Methods

2.1. Materials. All chemicals were ACS grade and purchased from commercial sources. The chemicals and materials used were polyvinylpyrrolidone (PVP) molecular weight of 40,000 (PVP40), iron sulfate heptahydrate ($FeSO_4 \bullet 7H_2O$), nickel chloride heptahydrate ($NiCl_2 \cdot 7H_2O$), Orange G dye, and sodium borohydride. Argon (99.9%) was commercially supplied, and aminotris(methylenephosphonic acid) (ATMP) was obtained from Dequest Italmatch Chemicals and used as received.

2.2. Synthesis. Nanoparticle synthesis was performed based on an aqueous chemical synthesis approach developed in a prior work [31–35]. Significant figures are reported based on measurement precision.

2.2.1. Core Shell Nanoparticle Synthesis. $FeSO_4 \cdot 7H_2O$ (124.6 g/L) dissolved in water is mixed with an ATMP (97 g/L) solution at 100 rpm while argon was bubbled into the mixture. $NaBH_4$ (44 g/L) in water was added to the $FeSO_4 \cdot 7H_2O$ and ATMP solution dropwise. The solution was placed under vacuum to remove excess hydrogen and mixed for 15 min. $NiCl_2 \cdot 7H_2O$ (100 g/L) was dissolved in water and mixed with PVP40 (100 g/L or 89.5 g/L, 39.8 g/L, and 17.9 g/L PVP40 concentrations with respect to $Ni_{10}Fe_{10}$, Ni_5Fe_{10}, and Ni_2Fe_{10} molar ratios) to make the $NiCl_2 \cdot 7H_2O$/PVP40. The $NiCl_2 \cdot 7H_2O$/PVP40 mixture was added to the $FeSO_4 \cdot 7H_2O$/ATMP/$NaBH_4$ solution and placed under vacuum again. The nanoparticles were centrifuged, supernatant was disposed, and nanoparticles were placed in argon-bubbled water.

2.2.2. Alloy Synthesis. $FeSO_4 \cdot 7H_2O$ (124.6 g/L) was dissolved in water and was mixed with an ATMP (97 g/L) solution at 100 rpm while argon was bubbled into the mixture. $NiCl_2 \cdot 7H_2O$ (100 g/L) was dissolved in water and mixed with PVP40 (100 g/L or 89.5 g/L, 39.8 g/L, and 17.9 g/L PVP40

concentrations with respect to $Ni_{10}Fe_{10}$, Ni_5Fe_{10}, and Ni_2Fe_{10} molar ratios) solution. The $NiCl_2{\cdot}7H_2O$/PVP40 mixture was added to the $FeSO_4{\cdot}7H_2O$/ATMP solution and bubbled with argon again. $NaBH_4$ (44 g/L) in water was added to the $FeSO_4{\cdot}7H_2O$/ATMP/$NiCl_2{\cdot}7H_2O$/PVP40 solution dropwise. The solution was placed under vacuum to remove excess hydrogen and mixed for 15 min. The nanoparticles were centrifuged, supernatant was disposed, and nanoparticles were placed in argon-bubbled water.

2.3. Orange G Removal Experiments

2.3.1. Procedure. The desired concentration of nanoparticles (1000 mg/L, 750 mg/L, 500 mg/L, and 250 mg/L) was syringed into a 60 mL test vial which already contained a 1 g/L Orange G dye solution. The vial was shaken by hand for no more than 2 seconds to mix the nanoparticles with the dye solution, and 1 mL was syringed from the vial and placed in a centrifuge tube (0 min time point). The mixture was then centrifuged, and the supernatant was pipetted into two wells of a well plate. The remaining supernatant was discarded. The sampling process was repeated every two minutes from the 0-minute time point to 20 minutes. From 20 minutes to the final 60-minute time point, samples were taken every 5 minutes. The samples were analyzed by an ultraviolet spectroscopy (UV-VIS) plate reader at 530 nm. The absorbances from this measurement were converted to concentrations using a standard curve, and a final graph of concentration versus time was produced for each experiment.

2.3.2. Shelf Life. A standard 60-minute time point test was repeated on each metal molar ratio of nanoparticles (alloy and core shell) every week for 0-3 weeks after the particles were synthesized. Samples were stored in argon-bubbled water during the entire 3-week experiment.

2.4. Characterization. The morphology of the nanoparticles was evaluated using a scanning electron microscope (SEM) operated at 20 keV. Samples were loaded into grids to dry before being placed into a vacuum chamber. Inductively coupled plasma mass spectrometry (ICP-MS) was used to detect the amount of metal (Ni and Fe) leached from the particles when placed in solution and determine the atomic ratio of metal : metal. Orange G degradation was confirmed through liquid chromatography mass spectrometry using a Synapt G2 HDMS from Waters Corp, using a Waters Acquity UPLC and C18 BEH analytical column.

3. Results and Discussion

3.1. Nanoparticle Characterization. The nanoparticles were synthesized with an aqueous batch method developed and discussed in the previous work [31, 32, 34, 35]. Representative images are shown in Figure S4 in Supplementary Materials. The morphology and structure of the NiFe nanoparticles are reported in prior publications [31, 33–35]. ICP was used to confirm desired (nickel : iron) molar ratios for the bimetallic nanoparticles, as shown in Table S1 in Supplementary Materials. ICP results indicate that when nanoparticles are synthesized in alloy morphology, the theoretical ratio of the iron and nickel precursors used during synthesis is quite similar to the measured ratio. The ratio increases slightly over time when the nanoparticles are stored, suggesting a small loss of iron from the nanoparticle composition with storage. However, for the core shell nanoparticles, the measured nickel to iron molar ratio is consistently lower than the theoretical ratio. This result occurs because the shell is formed through electroless deposition of the nickel cation precursor onto the iron core nanoparticle. Electroless deposition is arrested once a shell is formed, and a portion of the nickel precursor remains undeposited.

3.2. Azo Dye Degradation and Removal. The removal of Orange G was experimentally demonstrated through a measured decrease in dye absorbance using a UV-VIS spectrophotometer. Orange G degradation was confirmed through liquid chromatography mass spectrometry (LC-MS) (Synapt G2 HDMS from Waters Corp, using a Waters Acquity UPLC and C18 BEH analytical column) (Figure S3 in Supplementary Materials). Monometallic iron and nickel nanoparticles were initially tested for Orange G degradation over an hour period (Figure S2 in Supplementary Materials) as a comparison to the bimetallic nanoparticles. The iron nanoparticles react quickly to degrade the Orange G and become ineffective within the first minute. The nickel nanoparticles do not affect the overall dye concentration, unlike the iron nanoparticles. In comparison, bimetallic iron-nickel nanoparticles showed almost complete degradation of Orange G over an hour. Therefore, optimizing the bimetallic nanoparticle reactivity and stability was pursued for the rest of this study through an evaluation of nanoparticle: Orange G ratio, iron : nickel ratio, and nanoparticle morphology (core shell vs. alloy).

3.3. Effect of Nanoparticle Concentration on Azo Removal. All bimetallic nanoparticles synthesized in this study resulted in the same general trend over an hour of exposure to Orange G in a well-mixed batch reactor, as is illustrated for Ni_5Fe_{10} nanoparticles in Figure 1. However, the effect of nanoparticle concentration on dye removal is significant, and below a certain concentration threshold, the nanoparticles essentially become ineffective at dye removal. When a nanoparticle concentration of 250 mg/L is initially added to the 1 g/L Orange G solution, the nanoparticles at this concentration are able to remove the dye by only 20% or less. At 250 mg/L, a portion of the dye is removed within the first minute, and removal levels off over the rest of the hour. The nanoparticle concentrations of 500 mg/L, 750 mg/L, and 1000 mg/L follow the same trend of removing the dye within the first minute with degradation increasing until ~25 minutes and then leveling off for the remainder of the experiment. A nanoparticle concentration of 500 mg/L results in an overall Orange G degradation of approximately 60%. In contrast, nanoparticle concentrations of 750 mg/L and 1000 mg/L result in overall Orange G removal of about 85% and 95%, respectively. Therefore, the more concentrated solutions of nanoparticles used to treat Orange G improved dye removal for both nanoparticle morphologies.

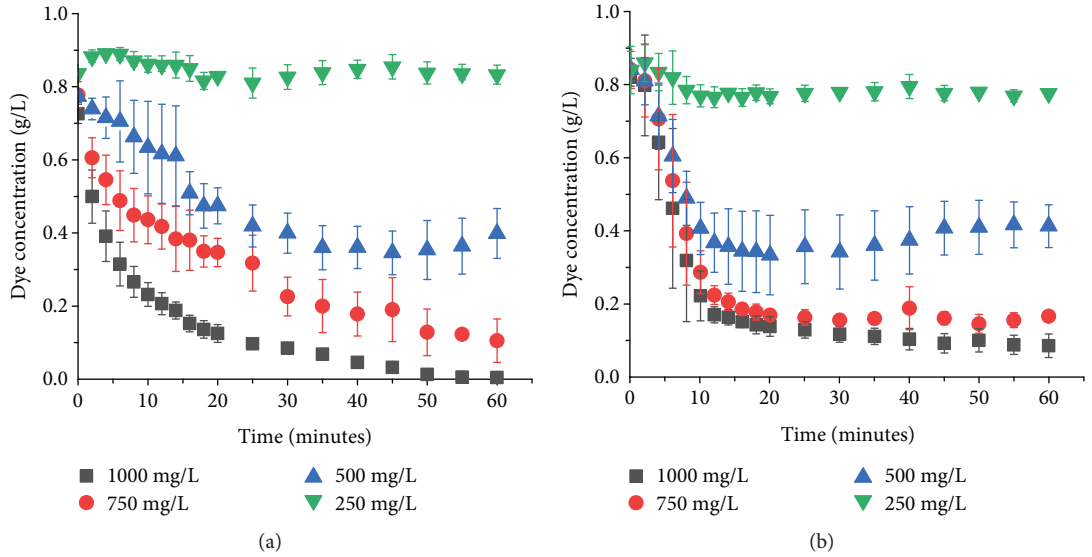

Figure 1: Effect of nanoparticle concentration for Ni_5Fe_{10} molar ratio nanoparticles on a 1 g/L dye concentration over time for the (a) alloy morphology and (b) core shell morphology.

3.4. Effect of Nickel Content on Azo Dye Degradation. The three molar ratios (Ni_2Fe_{10}, Ni_5Fe_{10}, and $Ni_{10}Fe_{10}$) for the bimetallic nanoparticles were tested using a starting nanoparticle concentration of 1000 mg/L to treat a 1 g/L Orange G solution. The removal trends are shown in Figure 2, and the degradation data is supported by mass spectrometry results summarized in Figure S3 and Table S2 in Supplementary Materials. Interestingly, there are different trends in the removal rate for the two different nanoparticle morphologies, as can be observed in Figures 2(a) and 2(b). Specifically, the core shell nanoparticles initially remove the dye by ~10% within the first minute, whereas the alloy nanoparticles initially degrade the dye by 20-30% within the first minute. The core shell nanoparticle removal rate begins to level off by ~20 minutes, unlike the alloy particles, which continually degrade dye until the end of the experiment. The last 40 minutes of treatment for both the core shell and the alloy nanoparticles is shown in Figures 2(c) and 2(d). The core shell nanoparticles result in a decrease in overall Orange G removal and degradation as the nickel amount is decreased (i.e., overall removal trends as $Ni_{10}Fe_{10}$ > Ni_5Fe_{10} > Ni_2Fe_{10}). Interestingly, the alloy nanoparticles did not follow the same trend as the core shell nanoparticles. Instead, the performance of the alloy nanoparticles was optimal in the Ni_5Fe_{10} composition for removal, but both Ni_2Fe_{10} and Ni_5Fe_{10} compositions resulted in the same overall degradation. However, the alloy nanoparticles were not drastically affected by the change in nickel content, resulting in only a standard deviation of ±0.006 g/L for the final dye concentration. These differences in how the nanoparticles perform result from the difference in nanoparticle morphology, which also influences the overall bimetallic composition of the nanoparticles.

However, it is unlikely that the difference in behavior is simply the result of different bimetallic compositions between the core shell and alloy morphologies. For example, the $Ni_{10}Fe_{10}$ core shell nanoparticles had a similar measured nickel to iron ratio as the Ni_5Fe_{10} alloy nanoparticles (Table S1 in Supplementary Materials), and these two samples did result in similar performance for the removal of Orange G. However, the Ni_2Fe_{10} alloy nanoparticles, with a lower measured nickel to iron ratio, outperformed the Ni_5Fe_{10} core shell nanoparticles. These results demonstrate that the bimetallic composition is important and that there may be an optimum composition for dye removal, but that composition is not the only important factor that dictates performance.

3.5. Effect of Nanoparticle Morphology on Azo Degradation. The three molar ratios (Ni_2Fe_{10}, Ni_5Fe_{10}, and $Ni_{10}Fe_{10}$) for both bimetallic morphologies were tested using a starting concentration of 1000 mg/L of nanoparticles to treat a 1 g/L Orange G solution. The overall removal of Orange G over time is shown for both core shell and alloy nanoparticles in Figure 2. Core shell particles present a steeper negative slope for dye removal over the first twenty minutes compared to the alloy nanoparticles. During the last 30 minutes of treatment, the core shell nanoparticles change removal rate depending on molar ratio, whereas the alloy nanoparticles present the same removal rate for all molar ratios. The dye removal results over the last 30 minutes of the experiment for all three molar ratios (i.e., Ni_2Fe_{10}, Ni_5Fe_{10}, and $Ni_{10}Fe_{10}$) for both core shell and alloy nanoparticles are shown in Figure 3. From these results, it is clear that the performance of the core shell nanoparticles is affected by both the initial concentration of nanoparticles used and the amount of nickel used as a shell. However, only the initial concentration of nanoparticles used drastically affects the ability of the alloy nanoparticles to remove Orange G dye.

Based on spectrophotometry measurements, the alloy nanoparticles consistently result in >95% overall removal, unlike the core shell nanoparticles, with overall removal in a range from 66% to 89%, depending on parameters. However, the $Ni_{10}Fe_{10}$ core shell nanoparticles with a starting

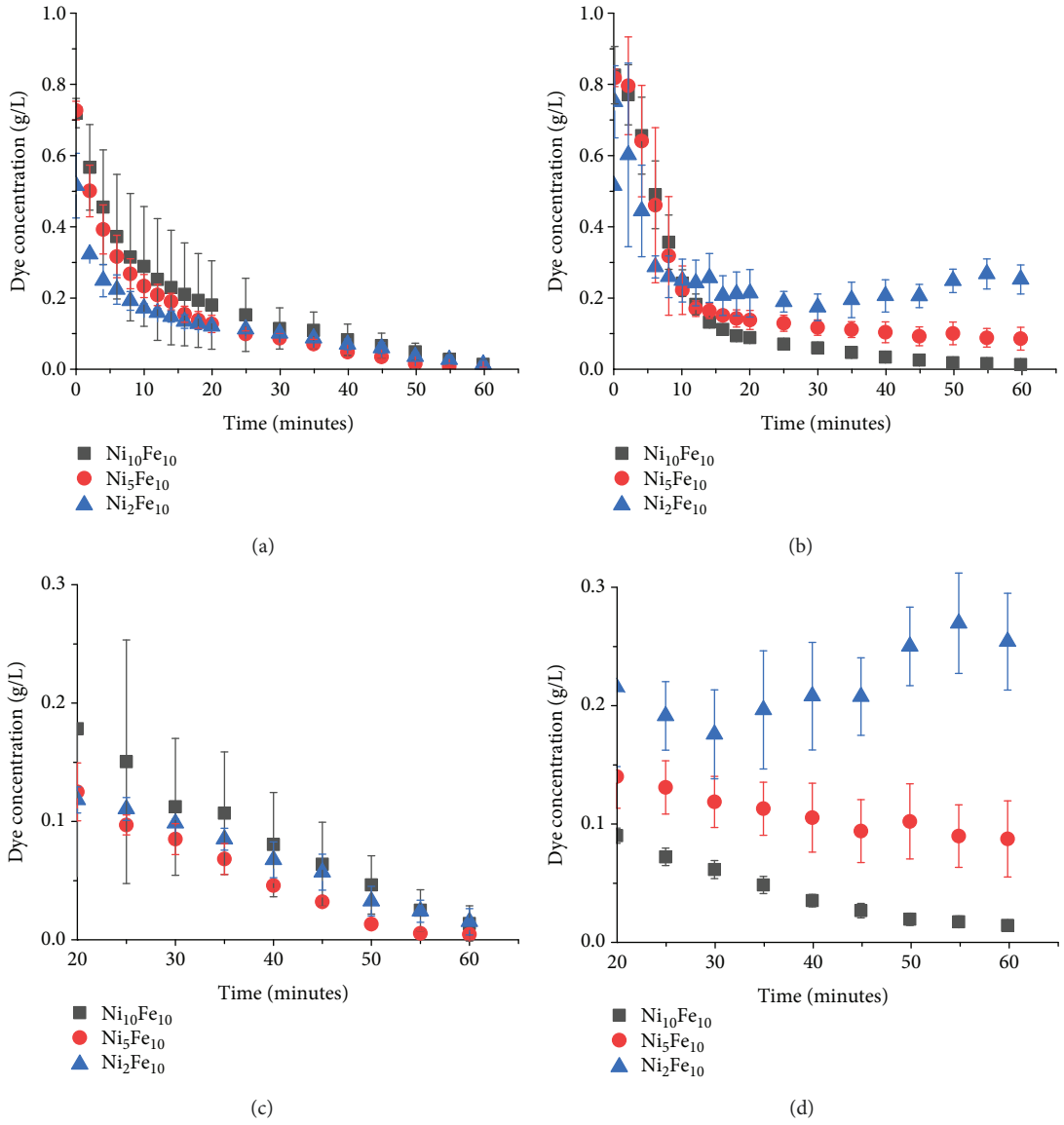

Figure 2: Effect of varying nickel content in (a) alloy nanoparticles and (b) core shell nanoparticles on the degradation of Orange G over time. The final forty minutes of treatment is shown in (c) for alloy nanoparticles and in (d) for core shell nanoparticles, demonstrating significant differences as a function of nanoparticle composition and morphology. All nanoparticles were tested at a concentration of 1000 mg/L.

concentration of 1000 mg/L reach 98%, which is comparable to the alloy nanoparticles. Interestingly, the mass spectrometry data suggest that all of the nanoparticle compositions, except for $Ni_{10}Fe_{10}$ alloy nanoparticles, achieve 99% removal of the dye within 60 min. One possible reason for this discrepancy in the data from UV-vis spectrophotometry versus mass spectrometry is that the spectrophotometry method may also measure color due to iron oxidation, which may be occurring later in the experiment as a result of reaction with nickel and with the dye [8, 36]. From the mass spectrometry data, results suggest that the higher nickel content of the $Ni_{10}Fe_{10}$ composition does not perform as well as the lower compositions in total dye removal or in the rate of removal. Further surface studies of the chemistry of the nanoparticles during and postreaction will need to be explored to understand these trends.

3.6. Effect of Storage Time on Azo Removal. The storage capability and lifetime of as-synthesized nanoparticles are important to understand when scale-up synthesis and production for use in pilot scale demonstrations are considered [25, 37–39]. The nanoparticles were stored at room temperature in argon-bubbled water and then were tested once a week for three weeks following the synthesis week (i.e., week zero). The results are shown in Figure 4 for core shell and alloy nanoparticles at starting concentrations of 1000 mg/L and 500 mg/L. Figure 4(a) shows that 1000 mg/L alloy nanoparticles remain reactive over a 3-week storage period, resulting in a standard deviation of ±0.017 g/L for all final Orange G concentrations for weeks 0 to 3. However, the 1000 mg/L and 500 mg/L core shell nanoparticles became less reactive over the 3 weeks. Surprisingly, the 500 mg/L (Figure 4(c)) alloy nanoparticles appeared to become more

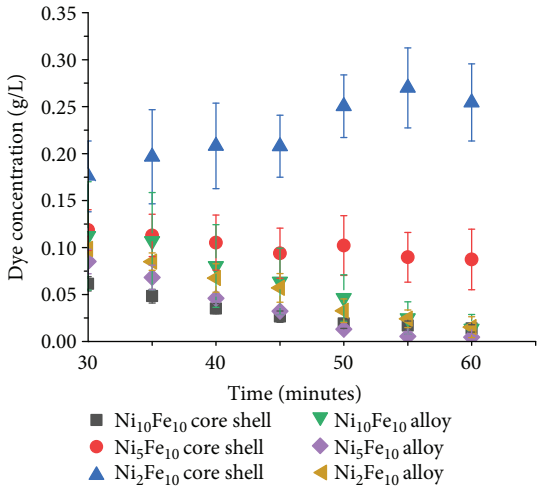

FIGURE 3: Comparison of 1000 mg/L core shell and alloy nanoparticles at three different nickel-iron ratios over the last thirty minutes of treatment.

reactive over the 3 weeks. Fresh 500 mg/L alloy nanoparticles removed only 42% of the dye; whereas, the same 500 mg/L alloy nanoparticles achieved 79% removal of the dye after the 3-week storage period. This change in the spectrophotometry results may suggest changes in dye removal, as well as changes to the nanoparticle chemistry that cause a change in the iron oxidation behavior; both factors could cause a change in the measured absorbance readings from spectrophotometry.

3.7. Nanoparticle-Driven Orange G Removal Kinetics. Removal of Orange G over time for each molar ratio, nanoparticle morphology, and starting nanoparticle concentration was fit to zero-order, first-order, and second-order reaction rate equations to determine the reaction rate order and rate constant for each experiment. Our results showed consistent results in terms of the reaction rate order over the 60-minute experiment. Specifically, each experiment presented a fit for the first 20 minutes (rate constant k_1) and a fit for the last 40 minutes (rate constant k_2). The data were not fit well to a single rate equation for the entire 60 min experiment, suggesting that there are two regions of Orange G decolorization and removal for all nanoparticle samples tested. Further, we observe a different reaction rate order for both regions for the different nanoparticle morphologies of alloy and core shell. The rate constant (second order, denoted as $k_{1,2}$) for alloy nanoparticles and the rate constant (first order, denoted as $k_{1,1}$) for core shell nanoparticles over the first 20 minutes are plotted as a function of nickel to iron molar ratio, starting nanoparticle concentration, shelf life/-storage, and morphology in Figures 5(a)–5(f). As can be seen from this set of graphs, not only are the rate orders different between the two morphologies, but also are the trends in k_1 quite different for alloy versus core shell morphologies. Individual plots of k_2 values as a function of nanoparticle properties are shown in Figure S5 in Supplementary Materials, where we observe that all rate constant values are less than 0.01 g/L/min. For all nanoparticles tested, the magnitude of k_1 is much greater than that of k_2. Values for k_1 are largely at least 10× greater in magnitude. From this result, we conclude that the majority of dye removal occurs within the first 20 min, and after 20 min, the nanoparticles result in little additional dye removal.

Nanoscale zero-valent iron (nZVI) has been generally shown to follow pseudo-first-order reaction kinetics for azo dyes such as Reactive Black 5 (RB5) [40], Acid Blue 113 [41], Acid Orange 07 [42], Allura Red [41], Amaranth [41], Orange G [41], Naphthol Blue Black [41], Orange I [41, 43], Orange II [41, 43], Sunset Yellow FCF [41], and Tartrazine [41]. However, Methyl Orange resulted in zero-order reaction kinetics [43]. A pseudo-first-order reaction rate assumes that the changing concentration of the dye controls the reaction rate, and the nanoparticle (i.e., iron) concentration is assumed to be constant. With the focus of extending nZVI lifetime through surfactant [40], granular activated carbon [42], and metal addition such as Ni [7, 8], there are a few studies on the kinetics of nickel-iron bimetallic nanoparticles. NiFe alloy nanoparticle catalysts were shown to fit a pseudo-first-order reaction rate for scarlet 4SB [28], Direct Black G [26], and Orange G [7, 8]. However, NiFe nanoparticles presented a pseudo-second-order reaction rate for Methyl Orange [27]. We note that both ZVI and NiFe studies on Methyl Orange resulted in different kinetic rate laws, as compared to multiple other tested dyes. Methyl Orange and Orange G both contain one azo dye linkage, suggesting that the number of azo linkages does not affect the kinetics, but the kinetics may be affected by the properties of the NiFe nanoparticles. Although the bimetallic NiFe nanoparticles used for Orange G and Methyl Orange were both nominal alloy morphologies, the difference in reaction kinetics indicates an importance of nanoparticle characteristics. The NiFe nanoparticles used for Methyl Orange had a molar ratio of $Ni_{2.5}Fe_{10}$, an average particle size of 12-16 nm, and a specific surface area of 34.93 m^2 g^{-1} and presented as flower-like nanostructures accompanied by nanorods [27]. The NiFe nanoparticles used for Orange G had a molar ratio of $Ni_{12}Fe_{10}$, an average particle size of 20-40 nm, and a specific surface area of 26 m^2 g^{-1} and presented as smooth spherical particles connected in chains [8]. The lower Ni concentration in the overall nickel-iron composition that was investigated with Methyl Orange dye corroborates our alloy nanoparticle second-order kinetic results; whereas, the higher Ni concentration followed the prior literature results of first-order kinetics. As we did not test equivalent higher nickel concentrations in our bimetallic alloy composition, it is possible that the order of the reaction rate might also change for our alloy nanoparticles at a higher nickel content. Currently, most of the NiFe nanoparticle literature and kinetic analyses only address alloy particles, and our results add to this literature through a comparative investigation of both core shell and alloy morphologies.

In our analysis, we initially exclude the nanoparticle concentration to analyze the kinetics of the dye removal as solely a function of dye concentration. This is a common assumption in ZVI-based literature on dye removal and may have limitations at low nanoparticle concentrations. This assumption holds true for core shell nanoparticles;

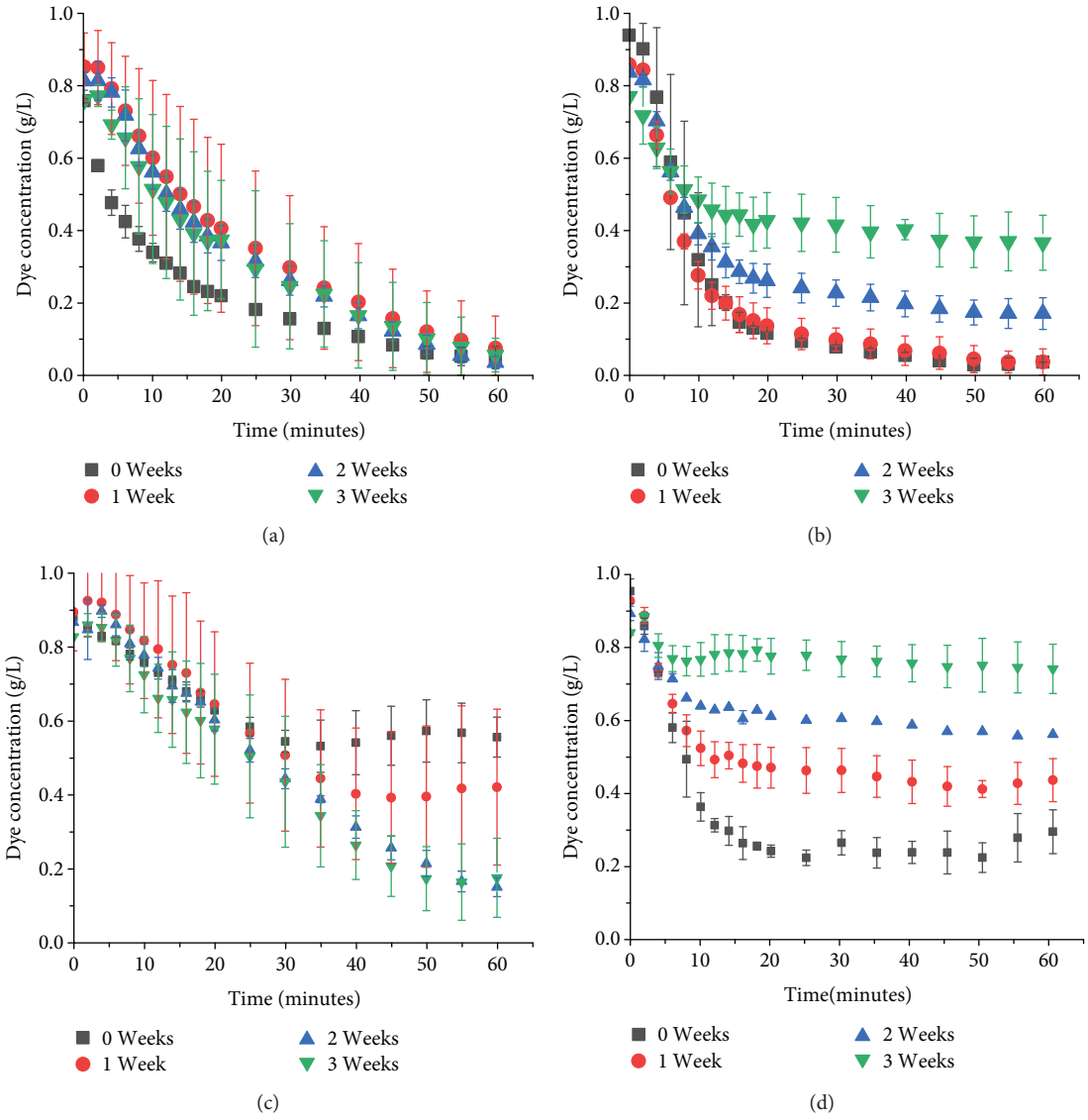

FIGURE 4: 1 g/L stock dye solution concentration over time for $Ni_{10}Fe_{10}$ molar ratio nanoparticles at different starting concentrations. (a) Alloy morphology with a starting nanoparticle concentration of 1000 mg/L. (b) Core shell morphology with a starting nanoparticle concentration of 1000 mg/L. (c) Alloy morphology with a starting nanoparticle concentration of 500 mg/L. (d) Core shell morphology with a starting nanoparticle concentration of 500 mg/L.

core shell nanoparticles fit a pseudo-first-order reaction rate for the first 20 minutes of removal and fit a zero order reaction rate for the last 40 minutes of removal. The first-order rate constant ($k_{1,1}$) is determined over the first 20 minutes and the zero order rate constant ($k_{2,0}$) over the last 40 minutes. In contrast, however, alloy nanoparticles fit a second-order kinetic rate for the first 20 minutes of removal and fit a zero-order reaction rate for the last 40 minutes of removal. The second-order reaction rate suggests that with alloy nanoparticles, there is a second-order rate dependence on the dye concentration; the nanoparticle concentration (or metal concentration) may also affect the reaction rate. The second-order rate constant ($k_{1,2}$) is determined over the first 20 minutes and the zero-order rate constant ($k_{2,0}$) over the last 40 minutes. The change in kinetics with time can be the result of adsorption limitations due to site deactivation or site blocking on the nanoparticle surface, along with oxidation of ZVI and loss of reactivity. The adsorption kinetics for a heterogeneous reaction is an important first step, since the chemisorption of the reactants on the catalyst surface can reduce the overall activation energy of the reaction [43]. However, the adsorption and reductive reaction of azo dyes occur simultaneously, making it difficult to predict adsorption.

The different kinetic trends for core shell and alloy suggest that the nanoparticle morphology affects how the Orange G dye is removed from solution. In general, a first-order reaction rate suggests that there is one reactive component concentration in solution that is directly correlated to the reaction kinetics. The concentration of Orange

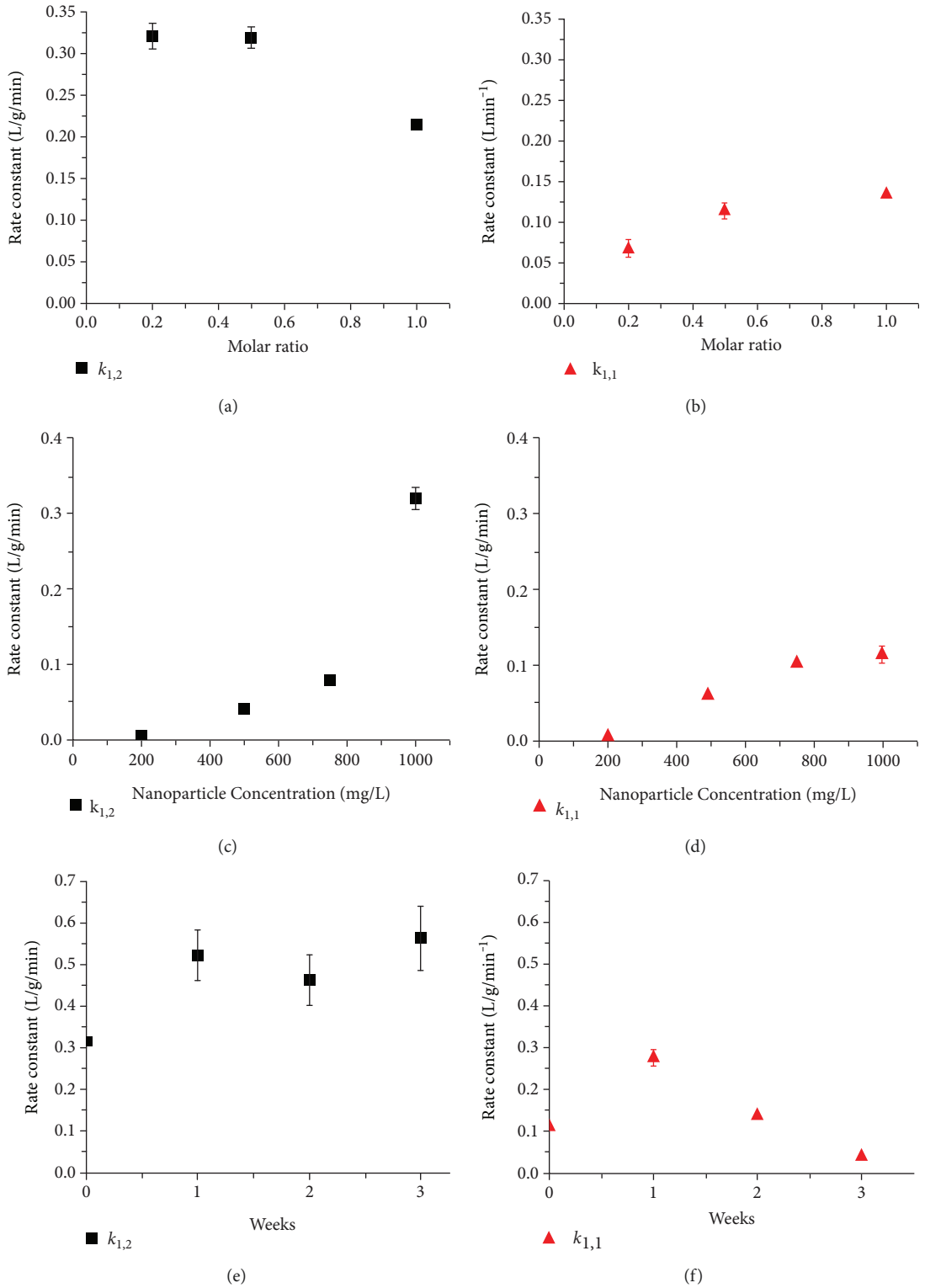

FIGURE 5: Second-order kinetic rate constants for 1000 mg/L alloy particles comparing (a) molar ratio, (b) particle concentration, and (c) reactive shelf life of Ni_5Fe_{10} alloy particles. First-order kinetic rate constants for 1000 mg/L core shell particles comparing (d) molar ratio, (e) particle concentration, and (f) reactive shelf life of Ni_5Fe_{10} core shell particles.

G dye is assumed to be the primary reactant that controls the reaction rate for first-order kinetics [8]. In second-order reactions, there are either two reactants that affect the reaction rate or a second-order dependence on one reactant. In the iron-nickel bimetallic system, the proposed reaction mechanism is quite complex [7, 8] and is proposed to include synergistic electron transfer between iron and nickel species, as well as both oxidative and reductive reaction steps with

Orange G dye [7, 8]. As a result, it is not possible to definitively separate the roles of iron and nickel, but our results as a function of NiFe molar ratio and nanoparticle concentration can be used to draw several qualitative conclusions as to what is driving the second-order reaction rate of the alloy nanoparticles.

First, the rate constant, $k_{1,2}$, remains essentially the same for the two lower molar ratios of Ni_2Fe_{10} and Ni_5Fe_{10}, and $k_{1,2}$ decreases for the highest molar ratio of $Ni_{10}Fe_{10}$ for the alloy nanoparticle morphology (Figure 5(a)). This result suggests that there is an optimum nickel content in these bimetallic systems, and too much nickel content in the Fe-based nanoparticle can be detrimental to the reaction rate. This suggestion is reinforced for the core shell morphology (Figure 5(d)) where the increase in nickel content (from Ni_2Fe_{10} to Ni_5Fe_{10}) results in a ~70% increase in reaction rate. However, Ni_5Fe_{10} to $Ni_{10}Fe_{10}$ shows only a ~19% increase in reaction rate constant, suggesting that the addition of nickel content is getting closer to the optimum level before a decline in reaction rate constant. Second, the rate constant, $k_{1,2}$, for alloy nanoparticles increases dramatically with increasing nanoparticle concentration (Figure 5(b)). The rate constant $k_{1,1}$ for core shell nanoparticles also increases with increasing nanoparticle concentration (Figure 5(e)). However, the core shell nanoparticles present a gradual, asymptotic increase in reaction rate constant as compared to the exponential increase of the alloy nanoparticles. This result is perhaps unsurprising and directly suggests that the reaction rate is dependent on the concentration of iron and nickel in nanoparticle form in the reaction solution. These results also demonstrate that the molar ratio of nickel to iron is important and that the second-order rate equation is perhaps a pseudo-second-order reaction, where the third "reactant" is a combination of the overall concentration of metals, as well as the specific ratio of nickel to iron for the alloy nanoparticles. As for the core shell nanoparticles, the first-order reaction kinetics suggest that the concentration of Orange G controls the reaction rate. However, the molar ratio of nickel to iron and the initial nanoparticle concentration result in different reaction rates when the Orange G concentration is held constant, demonstrating that molar ratio and nanoparticle concentration can positively affect reaction rates. Overall, molar ratio and nanoparticle concentration affect the removal of Orange G for both the alloy and core shell nanoparticles with a stronger influence on the alloy morphology.

The molar ratio of both alloy and core shell nanoparticles results in changes in rate constants (both $k_{1,1}$ and $k_{1,2}$) shown in Figures 5(a) and 5(b). However, alloy nanoparticles were found to have a higher average rate constant value (~0.28 L/g/min) for all of the molar ratios when compared to core shell nanoparticles (~0.08 min^{-1}). The starting nanoparticle concentration for the Ni_5Fe_{10} alloy and core shell nanoparticles was found to increase the kinetic rate constant with an increase in concentration as shown in Figures 5(b) and 5(e). The alloy nanoparticles present an exponential increase in kinetic rate constant value with an increase in nanoparticle concentration. The core shell nanoparticles present an increase in kinetic rate constant value with anincrease in nanoparticle concentration and the increase levels off at higher nanoparticle concentrations. This asymptote indicates that the nanoparticle concentration range (800–1000 mg/L) where the pseudo-first-order rate assumption holds and the nanoparticle concentration can be assumed to not impact the rate constant. At lower concentrations, based on our results, this assumption is likely not valid and a complete analysis of the rate constant would need to include the change in nanoparticle concentration (or the change in iron/nickel species) concentration. The shelf life over 3 weeks resulted in a change in kinetic rate constant values for both Ni_5Fe_{10} alloy and core shell nanoparticles as shown in Figures 5(c) and 5(f). The alloy nanoparticles were found to have a variable increase in kinetic rate constant without decreasing below the initial starting rate constant over a 3-week time. The core shell nanoparticles reached an optimum kinetic rate constant (0.23 min^{-1}) after 1 week and then steadily decreased to 0.03 min^{-1} kinetic rate constant by 3 weeks. Overall, the alloy nanoparticles result in larger kinetic rate constants and become increasingly larger with an increase in starting nanoparticle concentration and over time when compared to the core shell nanoparticles.

3.8. Nanoparticle Leaching. Nickel leaching has been occurring for decades in our water systems either through pipes, fittings, or naturally occurring nickel in rocks and sediments. Nickel is present in our environment, both water and soil, in low levels (microgram/liter), which also makes it hard to monitor. Nickel is essential and required in small quantities to sustain life. However, when intake of nickel is too high, it can be very dangerous leading to illness, cancer, and even death. Therefore, the Environmental Protection Agency has placed a maximum contaminant level (M_{cl}) of 0.1 mg/L on Ni in drinking water to prevent health issues.

Although Ni is the main concern for leaching, we investigated the loss of both Fe and Ni from the particles. The concentration of both Ni and Fe lost in solution over a 60-minute time period for all molar ratios (Ni_2Fe_{10}, Ni_5Fe_{10}, and $Ni_{10}Fe_{10}$) and both morphologies (core shell and alloy) is shown in Figure 6. Unfortunately, upon addition of the nanoparticles (core shell and alloy) to the solution, Ni is leached at the M_{cl} or in excess for all the nanoparticles. Similarly, Fe is lost from all of the nanoparticles upon addition at higher concentrations than 0.1 mg/L. Core shell nanoparticles lost more Ni as the molar ratio increased (i.e., as Ni content increased, Ni leaching increased), whereas the Fe leaching increased as the molar ratio decreased (i.e., as Ni content decreased, Fe leaching increased). The alloy nanoparticles gave a trend of decreasing Ni concentration in the sample over the test period for the $Ni_{10}Fe_{10}$. Initially, almost 14 mg/L of Ni was leached from the particles, but over a 60-minute time frame, the final Ni content was 5 mg/L. The reason for this decrease in Ni concentration may be due to precipitation of the nickel species on iron oxides formed in solution over time. Although upon addition to water, the $Ni_{10}Fe_{10}$ alloy particles lost a large concentration of Ni, the final concentration was close to both Ni_2Fe_{10} and Ni_5Fe_{10} alloy nanoparticles, where Ni leaching concentration constantly increased over time as expected. The $Ni_{10}Fe_{10}$ alloy

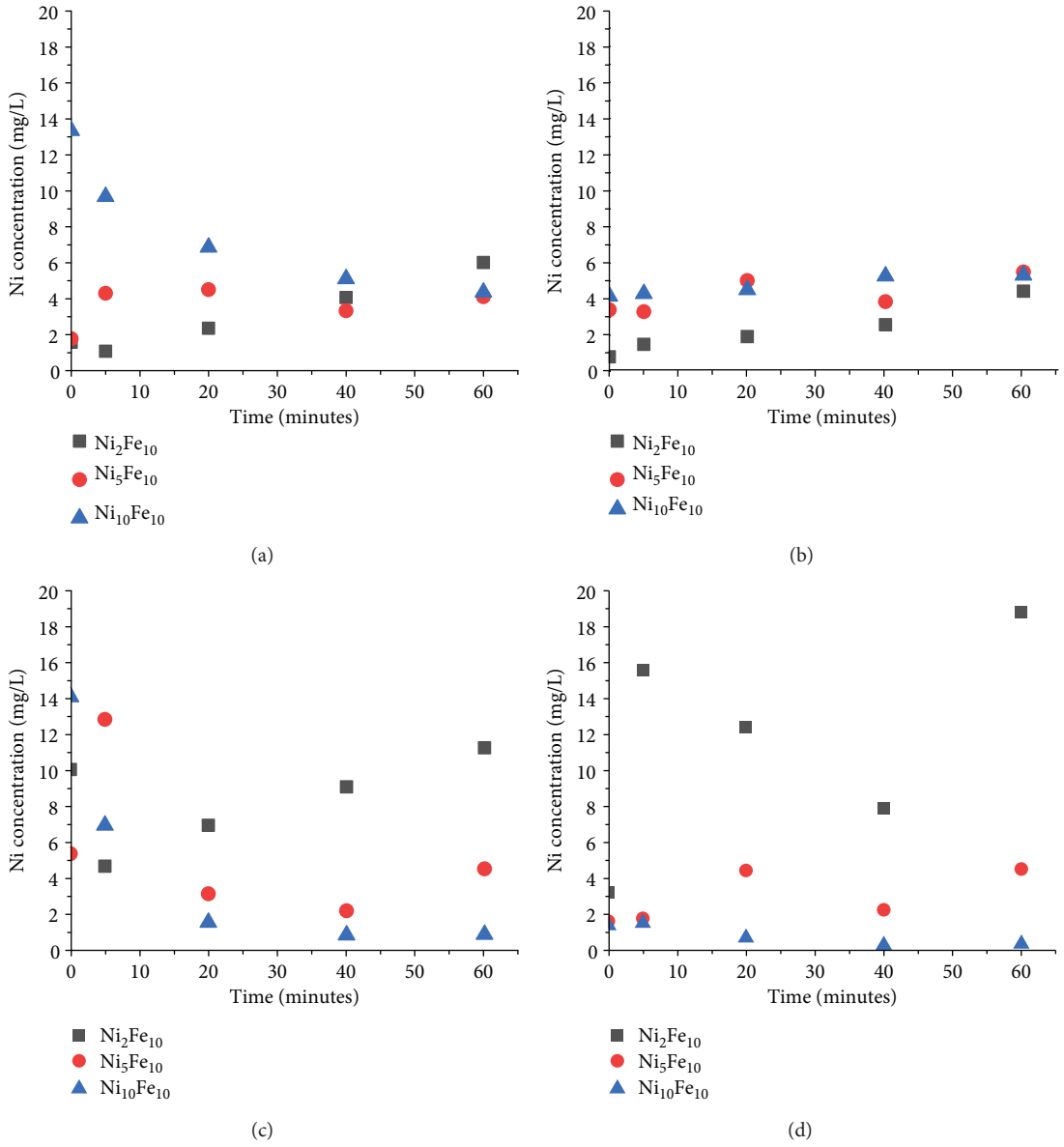

FIGURE 6: Amount of metal leaching from each molar ratio with a starting nanoparticle concentration of 1000 mg/L. Nickel leached over time from (a) alloy and (b) core shell particles. Iron leached over time from (c) alloy and (d) core shell particles.

nanoparticles present the same trend of high initial leached concentration to lower ending concentration for Fe leached over time, with oxidation and precipitation the likely mechanisms of removal. The Ni_5Fe_{10} alloy nanoparticles result in an increase in Fe leached concentration over the first ten minutes of testing and then decreased overall Fe leached to below the initial addition concentration ($t = 0$) over the next 30 minutes, with a final increase in concentration for the last 20 minutes. The Ni_2Fe_{10} shows an initial drop in Fe leached concentration from original addition to 10 minutes and then a steady increase in Fe leached concentration over the next 50 minutes. Based on these results, further stabilization of nanoparticles needs to be investigated to maintain both Ni and Fe concentrations throughout experiments. The results suggest that it is important to understand the roles of composition and morphology on leaching when evaluating this type of nanoparticle material for water treatment applications.

4. Conclusions

Core shell and alloy morphologies of a bimetallic NiFe nanoparticle were shown to remove an azo dye, Orange G, from water. Core shell nanoparticles resulted in an average removal rate of less than ~13% overall removal as compared to the alloy nanoparticles over 60 minutes. Both morphologies are directly affected by starting nanoparticle concentration, and the most effective treatment was obtained when nanoparticles were introduced to the reaction system at 1000 mg/L. The core shell nanoparticles are drastically affected by nickel concentration, resulting in a range of

removal from 66-98%, which corresponds to increasing nickel concentration in the nanoparticles. In contrast, the alloy nanoparticles were only slightly affected by nickel concentration, resulting in a smaller range of removal from 97-99%. The alloy nanoparticles were able to treat the dye just as effectively after 3 weeks of storage in water, while the core shell nanoparticles lost reactivity in each successive week. The morphologies presented different characteristics for removal and supported two different kinetic reaction models. The core shell nanoparticles followed a first-order reaction rate, while the alloy nanoparticles followed a second-order reaction rate over the first 20 minutes. However, both particle morphologies followed a zero-order reaction rate over the final 40 minutes. Overall, alloy nanoparticles at 1000 mg/L concentration, 0 weeks, and Ni_5Fe_{10} molar ratio resulted in the highest percent removal of ~99% over 60 minutes. All of the nanoparticles were found to leach undesired amounts of both Ni and Fe immediately upon addition to solution. Further investigation is needed for stabilization approaches through polymers, supports, or capping agents to keep Ni and Fe from dissolving into solution and causing both health concerns and decreased reactive lifetime.

Data Availability

The spectrophotometry, mass spectrometry, ICP, microscopy, and kinetic analysis data used to support the findings of this study are included within the article and within the supplementary information file.

Disclosure

This study is a contribution of NIST, an agency of the U.S. government, and is not subject to copyright in the United States.

Conflicts of Interest

The authors declare that they have no conflicts of interest.

Acknowledgments

The authors acknowledge help with ICP measurements, which were performed in the Department of Geological Sciences at the University of Colorado Boulder. The authors also acknowledge support from the Central Analytical Mass Spectrometry Facility at the University of Colorado Boulder, for help with LC-MS measurements. MV and KE acknowledge support from the Summer High School Internship Program (SHIP) at the National Institute of Standards and Technology. This work was supported by the National Institute of Standards and Technology and the University of Arkansas.

Supplementary Materials

Figures and tables of nanoparticle characterization, Orange G removal control experiment, mass spectrophotometry of Orange G degradation, and kinetic rate constants for the last 40 minutes of experiments are in the supplementary materials. *(Supplementary Materials)*

References

[1] M. A. Shaikh, "Water conservation in textile industry," *Pakistan Textile Journal*, vol. 58, pp. 48–51, 2009.

[2] K. A. Rade, V. A. Pharande, and D. R. Saini, "Effect of mass to liquor ratio on dyeing process," *Elixir Thermal Engineering*, vol. 89, pp. 36718–36722, 2015.

[3] F. M. Drumond Chequer, G. A. R. de Oliveira, E. R. Anastacio Ferraz, J. C. Cardoso, M. V. Boldrin Zanoni, and D. P. de Oliveira, *Textile Dyes: Dyeing Process and Environmental Impact*, Eco-Friendly Textile Dyeing and Finishing, IntechOpen, 2013.

[4] A. Gottlieb, C. Shaw, A. Smith, A. Wheatley, and S. Forsythe, "The toxicity of textile reactive azo dyes after hydrolysis and decolourisation," *Journal of Biotechnology*, vol. 101, no. 1, pp. 49–56, 2003.

[5] G. de Aragao Umbuzeiro, H. S. Freeman, S. H. Warren et al., "The contribution of azo dyes to the mutagenic activity of the Cristais River," *Chemosphere*, vol. 60, pp. 55–64, 2005.

[6] R. O. Alves de Lima, A. P. Bazo, D. M. Salvadori, C. M. Rech, D. de Palma Oliveira, and G. de Aragao Umbuzeiro, "Mutagenic and carcinogenic potential of a textile azo dye processing plant effluent that impacts a drinking water source," *Mutation Research*, vol. 626, pp. 53–60, 2007.

[7] A. D. Bokare, R. C. Chikate, C. V. Rode, and K. M. Paknikar, "Effect of surface chemistry of Fe–Ni nanoparticles on mechanistic pathways of azo dye degradation," *Environmental Science & Technology*, vol. 41, pp. 7437–7443, 2007.

[8] A. D. Bokare, R. C. Chikate, C. V. Rode, and K. M. Paknikar, "Iron-nickel bimetallic nanoparticles for reductive degradation of azo dye Orange G in aqueous solution," *Applied Catalysis B: Environmental*, vol. 79, pp. 270–278, 2008.

[9] H. M. Pinheiro, E. Touraud, and O. Thomas, "Aromatic amines from azo dye reduction: status review with emphasis on direct UV spectrophotometric detection in textile industry wastewaters," *Dyes and Pigments*, vol. 61, pp. 121–139, 2004.

[10] A. Subramani and J. G. Jacangelo, "Emerging desalination technologies for water treatment: a critical review," *Water Research*, vol. 75, pp. 164–187, 2015.

[11] W. L. Ang, A. W. Mohammad, N. Hilal, and C. P. Leo, "A review on the applicability of integrated/hybrid membrane processes in water treatment and desalination plants," *Desalination*, vol. 363, pp. 2–18, 2015.

[12] M. A. Oturan and J.-J. Aaron, "Advanced oxidation processes in water/wastewater treatment: principles and applications. A review," *Critical Reviews in Environmental Science and Technology*, vol. 44, pp. 2577–2641, 2014.

[13] B. P. Chaplin, "Critical review of electrochemical advanced oxidation processes for water treatment applications," *Environmental Science: Processes & Impacts*, vol. 16, no. 6, pp. 1182–1203, 2014.

[14] A. Babuponnusami and K. Muthukumar, "A review on Fenton and improvements to the Fenton process for wastewater treatment," *Journal of Environmental Chemical Engineering*, vol. 2, pp. 557–572, 2014.

[15] M. Punzi, A. Anbalagan, R. Aragão Börner, B.-M. Svensson, M. Jonstrup, and B. Mattiasson, "Degradation of a textile azo dye using biological treatment followed by photo-Fenton

oxidation: evaluation of toxicity and microbial community structure," *Chemical Engineering Journal*, vol. 270, pp. 290–299, 2015.

[16] C. R. Holkar, A. J. Jadhav, D. V. Pinjari, N. M. Mahamuni, and A. B. Pandit, "A critical review on textile wastewater treatments: possible approaches," *Journal of Environmental Management*, vol. 182, pp. 351–366, 2016.

[17] I. Ali, Z. A. Al-Othman, and A. Alwarthan, "Molecular uptake of congo red dye from water on iron composite nano particles," *Journal of Molecular Liquids*, vol. 224, pp. 171–176, 2016.

[18] T. Robinson, G. McMullan, R. Marchant, and P. Nigam, "Remediation of dyes in textile effluent: a critical review on current treatment technologies with a proposed alternative," *Bioresource Technology*, vol. 77, no. 3, pp. 247–255, 2001.

[19] V. K. Gupta and Suhas, "Application of low-cost adsorbents for dye removal – a review," *Journal of Environmental Management*, vol. 90, no. 8, pp. 2313–2342, 2009.

[20] X. Li, D. W. Elliott, and W. Zhang, "Zero-valent iron nanoparticles for abatement of environmental pollutants: materials and engineering aspects," *Critical Reviews in Solid State and Materials Sciences*, vol. 31, no. 4, pp. 111–122, 2006.

[21] Z. Wen, Y. Zhang, and C. Dai, "Removal of phosphate from aqueous solution using nanoscale zerovalent iron (nZVI)," *Colloids and Surfaces A: Physicochemical and Engineering Aspects*, vol. 457, pp. 433–440, 2014.

[22] J. Cao, L. Wei, Q. Huang, L. Wang, and S. Han, "Reducing degradation of azo dye by zero-valent iron in aqueous solution," *Chemosphere*, vol. 38, no. 3, pp. 565–571, 1999.

[23] L. Huang, X. Weng, Z. Chen, M. Megharaj, and R. Naidu, "Green synthesis of iron nanoparticles by various tea extracts: comparative study of the reactivity," *Spectrochimica Acta Part A: Molecular and Biomolecular Spectroscopy*, vol. 130, pp. 295–301, 2014.

[24] J. Fan, Y. Guo, J. Wang, and M. Fan, "Rapid decolorization of azo dye methyl orange in aqueous solution by nanoscale zero-valent iron particles," *Journal of Hazardous Materials*, vol. 166, pp. 904–910, 2009.

[25] H. Dong, Z. Jiang, J. Deng et al., "Physicochemical transformation of Fe/Ni bimetallic nanoparticles during aging in simulated groundwater and the consequent effect on contaminant removal," *Water Research*, vol. 129, pp. 51–57, 2018.

[26] X. Liu, Z. Chen, Z. Chen, M. Megharaj, and R. Naidu, "Remediation of Direct Black G in wastewater using kaolin-supported bimetallic Fe/Ni nanoparticles," *Chemical Engineering Journal*, vol. 223, pp. 764–771, 2013.

[27] H. Sarvari, E. K. Goharshadi, S. Samiee, and N. Ashraf, "Removal of methyl orange from aqueous solutions by ferromagnetic Fe/Ni nanoparticles," *Physical Chemistry Research*, vol. 6, pp. 433–446, 2018.

[28] Y. Lin, Z. Chen, M. Megharaj, and R. Naidu, "Degradation of scarlet 4BS in aqueous solution using bimetallic Fe/Ni nanoparticles," *Journal of Colloid and Interface Science*, vol. 381, pp. 30–35, 2012.

[29] N. Ezzatahmadi, T. Bao, H. Liu et al., "Catalytic degradation of Orange II in aqueous solution using diatomite-supported bimetallic Fe/Ni nanoparticles," *RSC Advances*, vol. 8, pp. 7687–7696, 2018.

[30] R. D. Kale and P. B. Kane, "Colour removal of phthalocyanine based reactive dye by nanoparticles," *Groundwater for Sustainable Development*, vol. 8, pp. 309–318, 2019.

[31] S. L. Candelaria, N. M. Bedford, T. J. Woehl et al., "Multi--component Fe–Ni hydroxide nanocatalyst for oxygen evolution and methanol oxidation reactions under alkaline conditions," *ACS Catalysis*, vol. 7, pp. 365–379, 2017.

[32] L. F. Greenlee, P. Acharya, and Z. Nelson, "Compositional optimization of alloy $Fe_xNi_y(OH)_2$ nanoparticles for alkaline electrochemical oxygen evolution," *ECS Transactions*, vol. 77, pp. 25–38, 2017.

[33] L. F. Greenlee and S. A. Hooker, "Development of stabilized zero valent iron nanoparticles," *Desalination and Water Treatment*, vol. 37, pp. 114–121, 2012.

[34] L. F. Greenlee and N. S. Rentz, "ATMP-stabilized iron nanoparticles: chelator-controlled nanoparticle synthesis," *Journal of Nanoparticle Research*, vol. 16, no. 11, p. 2712, 2014.

[35] L. F. Greenlee, J. D. Torrey, R. L. Amaro, and J. M. Shaw, "Kinetics of zero valent iron nanoparticle oxidation in oxygenated water," *Environmental Science & Technology*, vol. 46, pp. 12913–12920, 2012.

[36] V. Bokare, J.-l. Jung, Y.-Y. Chang, and Y.-S. Chang, "Reductive dechlorination of octachlorodibenzo-*p*-dioxin by nanosized zero-valent zinc: modeling of rate kinetics and congener profile," *Journal of Hazardous Materials*, vol. 250-251, pp. 397–402, 2013.

[37] F. He, D. Zhao, and C. Paul, "Field assessment of carboxymethyl cellulose stabilized iron nanoparticles for in situ destruction of chlorinated solvents in source zones," *Water Research*, vol. 44, pp. 2360–2370, 2010.

[38] R. L. Johnson, J. T. Nurmi, G. S. O'Brien Johnson et al., "Field-scale transport and transformation of carboxymethylcellulose-stabilized nano zero-valent iron," *Environmental Science & Technology*, vol. 47, pp. 1573–1580, 2013.

[39] P. K. Mondal, P. D. Furbacher, Z. Cui, M. M. Krol, and B. E. Sleep, "Transport of polymer stabilized nano-scale zero-valent iron in porous media," *Journal of Contaminant Hydrology*, vol. 212, pp. 65–77, 2018.

[40] S. Chatterjee, S.-R. Lim, and S. H. Woo, "Removal of Reactive Black 5 by zero-valent iron modified with various surfactants," *Chemical Engineering Journal*, vol. 160, pp. 27–32, 2010.

[41] S. Nam and P. G. Tratnyek, "Reduction of azo dyes with zero-valent iron," *Water Research*, vol. 34, no. 6, pp. 1837–1845, 2000.

[42] H. Liu, G. Li, J. Qu, and H. Liu, "Degradation of azo dye Acid Orange 7 in water by Fe^0/granular activated carbon system in the presence of ultrasound," *Journal of Hazardous Materials*, vol. 144, pp. 180–186, 2007.

[43] M. Hou, F. Li, X. Liu, X. Wang, and H. Wan, "The effect of substituent groups on the reductive degradation of azo dyes by zerovalent iron," *Journal of Hazardous Materials*, vol. 145, pp. 305–314, 2007.